Improved optoelectronic properties in CdSe$_x$Te$_{1-x}$ through controlled composition and short-range order

B.B. Dumre[a], N.J. Szymanski[a,b], V. Adhikari[a], I. Khatri[a], D. Gall[c], S.V. Khare[a,*]

[a] Department of Physics and Astronomy, University of Toledo, Toledo, OH 43606, USA
[b] Department of Material Science and Engineering, University of California, Berkeley, CA 94720-1760, USA
[c] Department of Materials Science and Engineering, Rensselaer Polytechnic Institute, Troy, NY 12180, USA

A B S T R A C T

We employ first principles methods based on density functional theory and beyond to study CdSe$_x$Te$_{1-x}$ alloys in the zincblende and wurtzite structures. From the cluster expansion formalism, we provide a detailed phase diagram showing a consolute temperature of 325 K, above which miscibility may be achieved. In the random solid solution, a zincblende-to-wurtzite phase boundary is found to range from Se concentrations of $x = 0.5$–0.6, in agreement with experiment, owing to increasing ionic character of the Cd-anion bonds. Disordered CdSe$_x$Te$_{1-x}$ configurations are modeled using special quasirandom structures, for which optoelectronic properties are computed with the hybrid HSE06 functional. Alloying is shown to cause strong bowing effects in the band gap and effective electron/hole masses, which we attribute to local structural distortions as illustrated by analysis of bond length distributions. Downward bowing in the band gap and effective hole mass of the zincblende structure is highlighted for its potential benefits in photovoltaics through increased net photocurrent. Absorption coefficients and reflectivity are also reported, showing promising results in zincblende CdSe$_x$Te$_{1-x}$ as indicated by substantial optical absorption throughout all Se concentrations. Lastly, we identify the presence of short-range order in CdSe$_x$Te$_{1-x}$ characterized by clustering among like atoms in order to minimize strain. The degree of clustering, which may be tuned by temperature, also controls the magnitude of the band gap. Therefore, we propose both composition and short-range order as effective tools to be utilized in the design and synthesis of improved solar cell absorber layer materials.

1. Introduction

Among thin film solar cell technologies, those based on CdTe as an absorber layer hold the largest market share owing to their robust longevity, high efficiency (~22%), and low cost (Green et al., 2018; Swanson et al., 2017; Zweibel, 1992). While the theoretical limit has been nearly achieved in the short-circuit current density (J$_{SC}$) of superstrate CdTe cells (Geisthardt et al., 2015), the corresponding open-circuit voltage (V$_{OC}$) is typically well below its potential maximum, displaying values of 0.84–0.88 V as opposed to the limit of ~1.2 V (Geisthardt et al., 2015; Gloeckler et al., 2013). As a result, the fill factor (FF) is decreased and the highest observed power conversion efficiencies (PCEs) lie ~10% below the 32% Shockley-Queisser limit (Shockley and Queisser, 1961) for CdTe-based photovoltaics (PV) (Green et al., 2018). To improve upon this constraint and climb the Shockley-Queisser curve, efficiency can be increased by decreasing the band gap through alloying with CdS, a commonly used window layer in

CdTe cells (Paudel and Yan, 2014). However, ~10% lattice mismatch (Terheggen et al., 2004) between CdS and CdTe keeps the solubility of dopants low, a high defect density in the graded CdTe$_{1-x}$S$_x$ layer increases carrier recombination rates (Gessert et al., 2013; Perrenoud et al., 2013), and thus parasitic absorption in wavelength range of 300–500 nm in CdS doesn't impart net photo-current (Romeo et al., 2004). In contrast, recent investigations have suggested that CdSe may be a more suitable choice to alloy with CdTe in hopes of increasing PCE (Green et al., 2018). While CdSe exists in the wurtzite ground state, CdSe$_x$Te$_{1-x}$ alloys have been shown to remain stable in either the zincblende (Islam et al., 1995; Uthanna and Reddy, 1983; Mangalhara et al., 1989) or wurtzite (Murali and Jayasuthaa, 2009; Belyaev and Kalinkin, 1988) structure depending on the concentration and temperature of synthesis. As the lattice mismatch of CdTe and CdSe is relatively small (~6% difference in lattice constant (Cai et al., 2012), the solubility of Se into Te is much higher than that of S, and the corresponding defect density is low, allowing for minimal effects on the

---

* Corresponding author.
  E-mail address: sanjay.khare@utoledo.edu (S.V. Khare).

recombination rate (Lingg et al., 2018). Although the band gap of CdSe (1.70 eV) (Kale and Lokhande, 2004) is higher than that of CdTe (1.50 eV) (Compaan et al., 1996), bowing effects cause the band gap to decrease at low to intermediate Se concentrations, resulting in enhanced PCE as the gap approaches the ideal Schockley-Queisser value (Hannachi and Bouarissa, 2008; Yang and Wei, 2019). Higher dopant levels may also be achieved in CdSe$_x$Te$_{1-x}$ as opposed to CdTe, which generally displays low carrier concentrations on the order of 10^{14} cm^{-3}, hence further increasing the possible photo-current (Kanevce et al., 2017). Additionally, as CdSe$_x$Te$_{1-x}$ spans a wide range of band gaps (1.3–1.7 eV), a graded absorber layer may be utilized to gain a greater degree of absorption throughout wavelengths in the visible spectrum (Jamal et al., 2016).

Though many papers (Swanson et al., 2017; Gloeckler et al., 2013; Gessert et al., 2013; Islam et al., 1995; Uthanna and Reddy, 1983; Mangalhara et al., 1989; Murali and Jayasuthaa, 2009; Belyaev and Kalinkin, 1988; Cai et al., 2012; Lingg et al., 2018; Baines et al., 2018; Poplawsky et al., 2016; Zhao et al., 2016; Strauss and Steininger, 1970) have been conducted to shed light on the properties and applications of the CdSe$_x$Te$_{1-x}$ system, some key issues need further investigation. Generally, experimental characterization of the binary CdTe-CdSe binary phase diagram has been constrained to high temperatures (Poplawsky et al., 2016; Strauss and Steininger, 1970). Hence, further work is needed to clarify the detailed phase stability of the zincblende and wurtzite structures throughout all temperatures and concentrations of interest. Moreover, theoretical methods may provide unique insight into the system by disentangling configurational and thermal contributions to the entropy, as well as temperature-dependent local bonding configurations, allowing a greater understanding into the underlying physics to be attained (Ozolins et al., 1998). With respect to the optoelectronic properties of CdSe$_x$Te$_{1-x}$ alloys, the majority of previous experimental works have focused on the zincblende structure (Hannachi and Bouarissa, 2008; Ouendadji et al., 2011; Shakil et al., 2016), while relatively little work has been done regarding the wurtzite phase (Reshak et al., 2011). As a result, an accurate tabulation of the band gaps and absorption coefficients remains absent for the wurtzite phase. While theory may be used to fill these gaps in data, the methods implemented must be chosen carefully. Recent works have shown that advanced techniques going beyond standard density functional theory, e.g., hybrid functionals, are necessary to accurately describe bowing effects of electronic properties in zincblende CdSe$_x$Te$_{1-x}$ (Yang and Wei, 2019). However, such methods remain untested with respect to the corresponding optical properties, for which the complete frequency- and compositional-dependence has yet to be characterized. Furthermore, effective electron and hole masses, which are crucial properties influencing the resulting photo-current and PCE (Granas et al., 2016), are unknown at intermediate concentrations. Should each of these properties be reported and their origin be understood, it may help clarify whether CdSe$_x$Te$_{1-x}$ represents an effective improvement upon conventional CdTe solar cells.

Throughout this work, we investigate the aforementioned issues by employing first principles methods to elucidate the fully detailed structural, thermodynamic, and optoelectronic properties of the CdSe$_x$Te$_{1-x}$ system in the zincblende and wurtzite structure. From analysis of calculations performed within the framework of the cluster expansion (CE) (Sanchez et al., 1984; Ducastelle and Ducastelle, 1991; De Fontaine, 1994; Zunger, 1994) and Monte Carlo (MC) (Newman and Barkema, 1999; Heermann, 1988; Dünweg and Landau, 1993; Laradji et al., 1995) formalisms, we characterize the phase stability of CdSe$_x$Te$_{1-x}$, showing that solubility may be achieved in the zincblende structure at low Se concentrations ($< 60\%$) and above moderate temperatures (~ 325 K). The miscibility gap at low temperatures is attributed to the minor lattice mismatch of CdTe and CdSe, illustrated through bond length analysis. Such variations in bond lengths also cause bowing of the band gap, for which predictive values calculated using the hybrid HSE06 functional are presented. Good agreement with

available experimental data is obtained. Calculated effective masses of electrons and holes are found to increase with Se concentration, which may limit photo current PCE. However, these effects may be offset at low Se concentrations by negative effective hole mass bowing, the potential for increased V$_{OC}$, and decreased reflectivity throughout the visible range. Furthermore, we find that short-range order, which correlates strongly with temperature shortly above the miscibility gap owing to covalent Te-Se interactions, may be utilized to finely tune the optoelectronic properties of CdSe$_x$Te$_{1-x}$ absorber layers.

2. Computational methods

All density functional theory calculations have been performed using the Vienna Ab initio Simulation package (VASP) (Kresse and Furthmuller, 1996; Kresse and Hafner, 1993; Kresse and Furthmuller, 1996; Kresse and Hafner, 1994). The projector augmented wave (PAW) method (Blochl, 1994; Kresse and Joubert, 1999) was employed with the generalized gradient approximation (GGA) in the form of the Perdew-Burke-Ernzerhof (PBE) exchange-correlation functional (Perdew et al., 1992; Perdew et al., 1993). Upon testing of convergence with respect to energy, a cutoff of 500 eV was chosen to be used for the plane-wave basis set. Default PAW potentials from the VASP library (Kresse and Furthmuller, 1996; Kresse and Hafner, 1993; Kresse and Furthmuller, 1996; Kresse and Hafner, 1994), including only the outer-core electrons as valence, were used for Cd, Te, and Se. Calculations were carried out on Γ-centered k-point meshes consisting of 4000 k-points per reciprocal atom (KPPRA). Electronic minimizations with a convergence criterion of 10^{-6} eV/atom were performed using the tetrahedron method with Blöchl corrections (Blöchl et al., 1994). Initial structural configurations of CdTe and CdSe in the zincblende and wurtzite structures were taken from the Materials Project (Jain et al., 2013) and geometrically optimized until forces acting on each atom were less than 0.01 eV/Å as mentioned in earlier works (Balasubramanian et al., 2016; Roehl and Khare, 2014; Roehl and Khare, 2014; Roehl et al., 2014; Warner et al., 2006; Zhou et al., 2014).

The MIT Ab initio Phase Stability (maps) code from the Alloy Theoretic Automated Toolkit (ATAT) was utilized to calculate CdTe-CdSe formation energy landscapes and binary phase diagrams within the cluster expansion formalism (van de Walle, 2009; van de Walle and Asta, 2002; van de Walle et al., 2002; van de Walle and Ceder, 2002). Vibrational contributions to the free energy were determined by calculating stiffness versus length relationships (van de Walle, 2013; van de Walle and Ceder, 2002) among 6 unique structures in the set enumerated by cluster expansion. For each structure, perturbations of magnitude 0.2 Å at 3 separate volumes were tested to obtain dynamical matrices, phonon spectra, and vibrational free energies. This information, collected using the fitsvsl and svsl codes in ATAT (van de Walle, 2009; van de Walle and Asta, 2002; van de Walle et al., 2002; van de Walle and Ceder, 2002), was used to modify the corresponding phase boundaries. Random Se/Te occupation occurring above the predicted consolute temperature was simulated with special quasirandom structures (SQSs) (Zunger et al., 1990), which were generated using the sqs2tdb code within ATAT (van de Walle, 2009; van de Walle and Asta, 2002; van de Walle et al., 2002; van de Walle and Ceder, 2002). To achieve the desired correlation parameters nearly matching those of the random configurations, CdSe$_x$Te$_{1-x}$ SQSs were constructed from $2 \times 2 \times 2$ supercells of the conventional zincblende and wurtzite unit cells at concentrations of x = 0.25, 0.50, and 0.75. These structures were geometrically optimized until forces acting on each atom were less than 0.01 eV/Å.

As band gaps and absorption onsets are severely underestimated by standard exchange-correlation functionals, e.g., GGA and LDA, we instead employ the Heyd-Scuseria-Ernzerhof hybrid functional (HSE06) (Heyd et al., 2003; Krukau et al., 2006) to calculate the optoelectronic properties of CdSe$_x$Te$_{1-x}$. The HSE06 functional, which incorporates 25% of the exact exchange from Hartree-Fock theory along with 75% of

the exchange from GGA, has been shown to give significantly improved agreement with experiment for semiconductors and insulators (Paier et al., 2006). Using this method, for which the exact exchange was treated on a coarser grid of 2000 KPPRA to conserve computational resources, we calculated the electronic density of states (DOS) and frequency-dependent complex dielectric function ($\varepsilon_1 + i\varepsilon_2$) for each compound, including both end members and SQSs. From the latter values, derived optical properties such as absorption coefficient and reflectivity were determined. To gain further insight into the optoelectronic properties, effective masses of electrons and holes were calculated using the BoltzTraP package (Madsen and Singh, 2006) along with the corresponding modules implemented in pymatgen (Ong et al., 2013). We report DOS effective masses as described in the work of Gibbs et al. (2017), allowing a holistic representation of the entire Fermi surface to be presented while avoiding explicit calculations of the band structure. These calculations were carried out using carrier densities of 10^{16} electrons or holes per cm^3, in accordance with the most recent limits reported in the literature for CdTe thin films (McCandless et al., 2018). Units are in terms of the standard electron rest mass ($m_0 \approx 9.11 \times 10^{-31}$ kg), i.e., the effective electron mass is $m^* = m_e/m_0$ (and similar for holes, m_h).

To investigate short-range order effects occurring in the Te/Se sublattice of $CdSe_xTe_{1-x}$ structures for which no long-range order exists, we focus on the intermediate concentration of x = 0.5. Here, Monte Carlo simulations are performed on 4096-atom supercells using the Easy Monte Carlo Code (emc2) within ATAT (van de Walle, 2009; van de Walle and Asta, 2002; van de Walle et al., 2002; van de Walle and Ceder, 2002). As the zincblende structure is predicted to be thermodynamically stable at this concentration, with a consolute temperature of 325 K, we test only zincblende $CdSe_{0.5}Te_{0.5}$ at temperatures ranging from 350 K to 1000 K, in steps of 50 K. To characterize the degree of short-range order present within each structure, we employ two techniques of analysis. Firstly, we compare the distribution of Se-Te coordination values occurring throughout all sites with the corresponding values of a completely disordered Se/Te configuration. Such comparison is approximated by randomly sorting occupations among 20 unique structures and averaging the resulting distributions of coordination values. Secondly, we define the following short-range order parameter for Se-Te pairs (Porter et al., 2009):

$$\sigma(T) = (N_{actual}^{Te-Se} - N_{random}^{Te-Se})/(N_{ordered}^{Te-Se} - N_{random}^{Te-Se}) \qquad (1)$$

where N_{actual}^{Te-Se}, $N_{ordered}^{Te-Se}$, and N_{random}^{Te-Se} represent the number of Te-Se bonds in the actual configuration simulated at some intermediate temperatures (T = 350 K, 1000 K), the ordered configuration (with each Cd coordinated to an equal number of Te and Se atoms) at absolute zero temperature, and the completely random configuration approached at very high temperatures (T ≫ 1000 K) in $CdSe_{0.5}Te_{0.5}$. By defining short-range order as such, positive and negative values of σ (max. +1 or −1) correspond to additional or reduced Te-Se bonds relative to the random limit, whereas a value of zero implies complete disorder.

Lastly, to provide further insight into electronic structure, we have performed calculations of Crystal Orbital Hamiltonian Populations (COHP) and effective charges using the LOBSTER package (Deringer et al., 2011; Maintz et al., 2013; Maintz et al., 2016; Maintz et al., 2016) and Bader analysis (Henkelman et al., 2006; Sanville et al., 2007; Tang et al., 2009; Yu and Trinkle, 2011) respectively.

3. Results

3.1. Phase stability of $CdSe_xTe_{1-x}$

Formation energy landscapes of $CdSe_xTe_{1-x}$ in the zincblende and wurtzite structure are displayed in Fig. 1(a) and (b) respectively. Both structures are found to exhibit endothermic mixing with upward bowing occurring in all enumerated configurations at intermediate concentrations, in agreement with recent theoretical work (Yang and
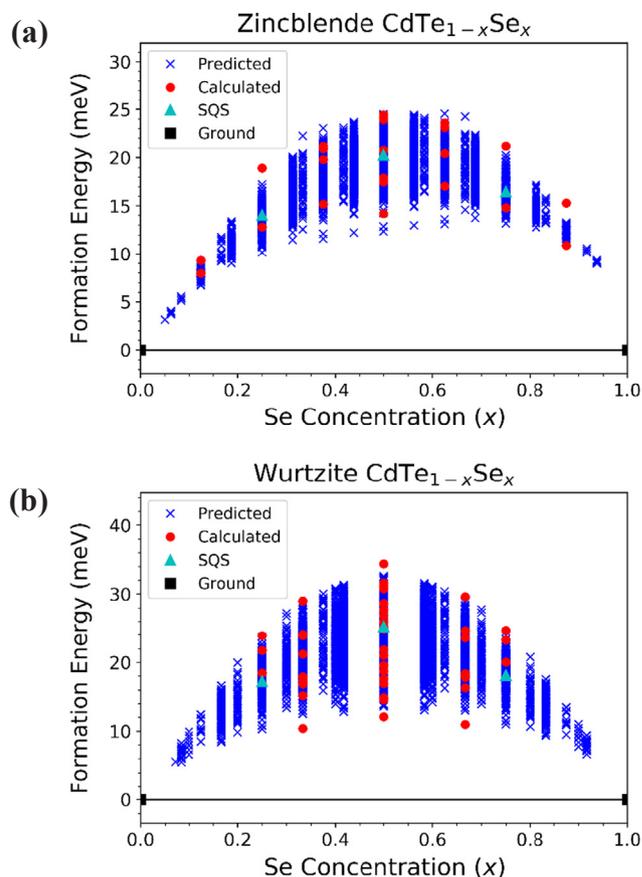

Fig. 1. Energy landscapes of (a) zincblende and (b) wurtzite $CdTe_{1-x}Se_x$, including ground states CdTe and CdSe, intermediate states predicted through cluster expansion and calculated using DFT, and special quasirandom structures simulated at concentrations of x = 0.25, 0.50, and 0.75.

Wei, 2019). The preference towards heterogeneity can be attributed to the CdTe/CdSe lattice mismatch arising from the difference in ionic radii of Te and Se (133.5 pm and 114.5 pm respectively) (Pyykkö, 2015). As the mismatch is relatively minor in contrast to that of CdTe/CdS, only slight asymmetry is observed in the energy landscape studied here. More specifically, upward bowing is weakly skewed towards higher Se concentrations as greater strain is caused by inserting the larger Te atoms into the CdSe lattice than vice versa, a well-studied effect in solid solutions (Liu et al., 2017). Regarding differences in structure, the wurtzite phase exhibits a larger rise in enthalpy than the zincblende phase; the former reaches a maximum ΔE_F of about 35 meV/atom whereas the latter achieves only 25 meV/atom. These features correlate with a greater volume difference of 9.0% in the wurtzite structure as opposed to 8.8% in the zincblende. Furthermore, the wurtzite configuration, for which c/a changes from 1.638 to 1.632 for CdTe and CdSe respectively, introduces a shear strain component not present in the cubic zincblende phase. As a result of these properties, solid solubility is less favorable in the wurtzite structure. Though we also note the anisotropy of the wurtzite phase is slightly more accommodating to low concentrations of larger impurity atoms, shown by weaker skewing of the energy landscape in contrast to that of the zincblende structure, owing to expansions along the c-axis which will be discussed in more detail throughout Section 3.2.

The binary $CdSe_xTe_{1-x}$ phase diagram is presented in Fig. 2. Throughout intermediate concentrations at low temperatures, phase segregation is thermodynamically favorable due to the endothermic mixing discussed for the corresponding formation energy landscapes. However, as the upward bowing in energy is relatively weak, configurational and vibrational contributions (both included here) to the
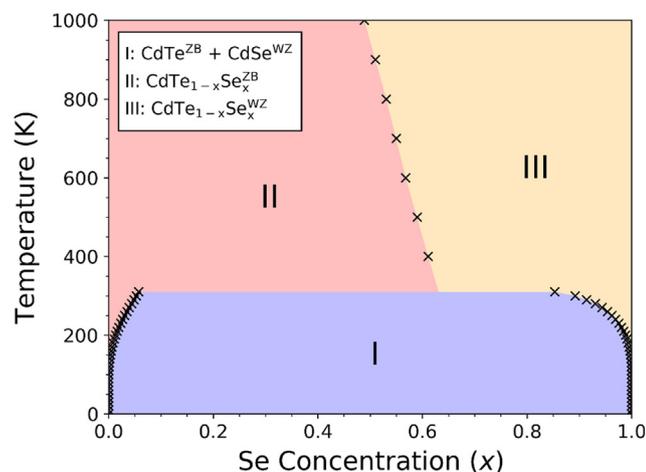
Fig. 2. The binary $CdTe_{1-x}Se_x$ phase diagram generated from Monte Carlo simulations utilizing effective cluster interaction coefficients.

entropy become sufficient to allow homogenous Se/Te mixing above a reasonably low consolute temperature (T_C) of about 325 K. As experimental synthesis is typically carried out at much higher temperatures (500–1000 K) (Lingg et al., 2018; Baines et al., 2018; Poplawsky et al., 2016), a precise value of T_C has not yet been reported. However, previous studies have shown that weak CdTe-CdSe phase segregation may proceed at room temperature (~298 K) depending on the thickness of deposition layers (Poplawsky et al., 2015). Moreover, recent theoretical investigations have predicted a similar T_C of 335 K using Stillinger-Weber Hamiltonian in molecular dynamics simulations (van Swol et al., 2016). In the high-temperature region of the phase diagram, we find the disordered $CdSe_xTe_{1-x}$ phase to adopt the zincblende and wurtzite structure at low and high Se concentrations respectively, with a downward-sloping phase boundary ranging from $x \sim 0.45$ to $x \sim 0.65$. These features are in good agreement with experimental data (Poplawsky et al., 2016; Strauss and Steininger, 1970; Laugier, 1973). We note that although the zincblende phase does not represent the thermodynamic ground state of $CdSe_xTe_{1-x}$ at high Se concentrations, our calculations reveal a difference of less than 10 meV/atom between the zincblende and wurtzite structures of CdSe, suggesting that the optically active (Poplawsky et al., 2016) zincblende phase may be synthetically accessible and remain metastable throughout a wide range of concentrations. This prediction is supported by recent experimental work showing $CdSe_xTe_{1-x}$ to remain stable against decomposition at Se concentrations as high as 60% at temperatures of 298 K and above (Lingg et al., 2018).

Regarding the zincblende-to-wurtzite phase transition, we discuss two major causes which have been suggested in previous works describing such structural polymorphism in binary octet semiconductors (Yeh et al., 1992; Ito, 1998). Firstly, the wurtzite structure is generally preferred over zincblende for binary compounds consisting of constituent elements with a substantial electronegativity difference (Yeh et al., 1992). Here, Se and Te display electronegativities of 2.48 and 2.01 respectively as compared to a value of 1.46 for Cd (Allred and Rochow, 1958), hence the Cd-Se bonds display significantly higher ionic character than the Cd-Te bonds. This is reflected by our Bader's charge analysis calculations which yield 0.71 e and 0.52 e cation-to-anion transfer in CdSe and CdTe respectively, where e is the elementary electron charge. As a result of the enhanced volumetric charge surrounding ions in CdSe, the wurtzite structure (with stacking sequence ABAB… as opposed to ABCABC… for zincblende) is adopted to minimize interlayer third-nearest-neighbor Cd-Se distances and therefore decrease overall energy deriving from attractive long-range electrostatic interactions ($U_E \propto r^{-1}$) (Ito, 1998). Secondly, as the ionic radius of Se (114.5 pm) is smaller than that of Te (133.5 pm), CdSe exhibits a

greater cation-anion size mismatch than CdTe due to the large ionic radius of Cd (148.2 pm) (Pyykkö, 2015). As shown in data from the literature, binaries with higher cation-to-anion size ratios tend to form wurtzite configurations owing to subtle differences in covalent interactions controlled by the relative spatial extent of the cation d and anion p orbitals (Yeh et al., 1992). However, as shown in Fig. S3 of the Supplementary Material, we find no significant differences in general features of the COHP curves when comparing the zincblende and wurtzite structures. Moreover, integration of all states below the Fermi level yields nearly identical values, implying covalent interactions of approximately equal strength in each structure. Therefore, we conclude that the preference of stacking sequence in $CdSe_xTe_{1-x}$ is likely dominated by the ionic character of the system.

Lastly, we note that the inclusion of entropic terms to the free energy were crucial to obtain the reported phase diagram for which satisfactory agreement with experimental data is obtained (Poplawsky et al., 2016; Strauss and Steininger, 1970; Laugier, 1973). This highlights the importance of both configurational and vibrational entropy in stabilizing the given configurations. Specifically, including these terms caused a substantial shift in the zincblende-wurtzite phase boundary towards lower Se concentrations, suggesting greater entropy contributions present in wurtzite $CdSe_xTe_{1-x}$ arising from larger average bond lengths and therefore lower vibrational frequencies. This property is also reflected by the downward slope of the phase boundary, which indicates the wurtzite structure may be stabilized at intermediate concentrations by increasing temperature and therefore enhancing the effects of vibrational entropy (Poplawsky et al., 2016).

3.2. Properties of anion-disordered $CdSe_xTe_{1-x}$

In order to understand the deviation from linearity, let's first define bowing parameter (δ) for any physical quantity (p) such as lattice constant (a), band gap (E_g), effective mass (m^*), or others as (Kasper et al., 1995):

$$p_{mix} = x_{Se}p_{CdSe} + (1 - x_{Se})p_{CdTe} - x_{Se}(1 - x_{Se})\delta_p, \qquad (2)$$

where x_{Se} is fraction of Se in the alloy and, p_{mix}, p_{CdSe} and p_{CdTe} are values of the physical quantity associated with resultant alloy, CdSe and CdTe respectively.

We first study the structural features of anion-disordered $CdSe_xTe_{1-x}$ as a function of concentration. As shown by the calculated equilibrium lattice parameters, presented in Table S1 of the Supplementary Material, the lattice constants and unit cell volumes follow nearly linear relationships, i.e. they approximately following Vegard's law (Vegard, 1921). The unit cell volumes decrease with average slopes of -12.659 and -12.908 Å^3 f.u.$^{-1}$ x^{-1} for the zincblende and wurtzite structure respectively. The bowing parameter δ_a is found to be -0.01 Å, -0.004 Å, and -0.008 Å for zincblende, wurtzite in-plane (a), and wurtzite out-of-plane (c) lattice constants respectively using Eq (2) with p = a. This deviation from Vegard's law is likely to arise from the additionally degree of freedom introduced by the anisotropy of the wurtzite structure. Indeed, larger changes occur in the c-axis relative to the a-axis in order to accommodate for the varying anion size and electronegativity. For instance, a larger 3.26% contraction of the c-axis occurs in contrast to a smaller 2.99% contraction of the a-axis at 50% Se concentration relative to pure CdTe in the wurtzite structure. These changes may be summarized by analyzing the ratio of c/a, tabulated for each concentration in Table S1, showing a decrease from 1.638 for CdTe to 1.632 for CdSe. The observed trend is consistent with previous findings for similar systems in the wurtzite structure; as the Se concentration is increased and ionic character of the cation-anion bonds becomes stronger, the ratio of c/a approaches the ideal value of 1.632 for a perfectly covalent crystal (Kim et al., 2007).

To gain further insight into the local structural features of $CdSe_xTe_{1-x}$, we have plotted bond length distributions in Fig. S1 of the Supplementary Material. As expected, anion disorder leads to

distortions in the Cd-anion tetrahedra corresponding to deviations from the ideal bond length; specifically, a clear distinction is found between the nearest-neighbor Cd-Te and Cd-Se distances with the former pairs exhibiting a median value which is nearly 0.15 Å larger than that of the latter. Such distortions, both within and between unique bonding pairs (Cd-Te and Cd-Se), also become slightly more pronounced at intermediate concentrations ($x \sim 0.5$) owing to increased strain induced by the differing anion sizes. As will be discussed further in this section, the bond length variations play a vital role in causing optoelectronic bowing effects and may therefore be utilized to control these properties (Tit et al., 2009). Also plotted in Fig. S1 is the nearest-neighbor anion-anion bond lengths, for which we find much weaker, though still present, differences between the grouping of unique bonding pairs, i.e., Te-Te, Te-Se, and Se-Se distances. These values correlate with the sum of constituent anionic radii, though local distortions in the tetrahedra have greater effect as shown by a wide (~ 0.38 Å) and continuous range of bond lengths. These properties and their connection to short-range order will be discussed in greater detail throughout Section 3.3.

We next study the electronic properties of $CdSe_xTe_{1-x}$ using the hybrid HSE06 (Heyd et al., 2003; Krukau et al., 2006) functional, where sample cells, x = 0.25, 0.5, 0.75, were generated with SQS as described in Section 2. With respect to end-members, zincblende CdTe and CdSe are shown to exhibit band gaps of 1.54 eV and 1.61 eV respectively, in fair agreement with experimental data of 1.50 eV (Compaan et al., 1996) and 1.78 eV (Poon et al., 1995). In contrast, the calculated band gaps of 1.23 eV and 1.32 eV for CdTe and CdSe in the wurtzite structure underestimate the corresponding experimental values of 1.59 eV (Magnusson et al., 1987) and 1.70 eV (Kale and Lokhande, 2004), though accuracy is significantly improved with respect to GGA (Table S2 of the Supplementary Material). The increased error occurring in the wurtzite structure, which is consistent with previous theoretical reports involving CdSe (Szemjonov et al., 2014) and similar binary semiconductors of equivalent symmetry (Moses et al., 2011; Kaczkowski, 2012), can be attributed to the short-range nature of the exact exchange implemented within the HSE06 (Heyd et al., 2003; Krukau et al., 2006) functional, which therefore may not capture long-range interactions arising from differences in the stacking sequence of each structure, i.e., zincblende (ABCABC…) vs. wurtzite (ABAB…). As discussed in the work of Moses et al., improvement with experiment may be obtained by tuning the portion of exact exchange interactions included in the hybrid calculations (Moses et al., 2011), however, we choose to keep parameters fixed to remain consistent across the distinct compositions and structure considered in this work. Moreover, although the magnitude of the band gap is underestimated in the wurtzite structure, we note that the change in gap with respect to composition agrees well with experiment; our calculations reveal an increase of 0.09 eV (experimentally, 0.11 eV (Kale and Lokhande, 2004; Magnusson et al., 1987) from CdTe to CdSe. Therefore, predicted changes in the electronic properties at intermediate concentrations may be considered reliable.

Accordingly, the calculated trend of band gap variation in $CdSe_xTe_{1-x}$ is displayed in Fig. 3(a) with exact values reported in Table S2 of the Supplementary Material. In both the zincblende and wurtzite phases, we find significant downward bowing to occur throughout intermediate concentrations. Specifically, our results indicate bowing parameters (δ) as defined in Eq. (2) (with p = E_g) of 0.62 eV and 1.06 eV for the zincblende and wurtzite phases respectively, for which the former results is in fair agreement with recent experimental (Islam et al., 1995) and theoretical (Yang and Wei, 2019) investigations regarding $CdSe_xTe_{1-x}$ in the zincblende structure. These trends can be attributed to local distortions arising in the disordered solid solution (Vurgaftman et al., 2001). Hence, the stronger bowing effect found in the wurtzite structure, as compared to zincblende, can be attributed to the larger lattice mismatch (i.e., volume difference) which is observed between the wurtzite CdTe and CdSe phases as discussed in Section 3.1. This greater mismatch causes enhanced structural distortions, as reflected by our bond length analysis (Fig. S1) which shows slightly wider

ranges of Cd-anion bond lengths at intermediate concentrations for the wurtzite phase. Moreover, the larger volume of the wurtzite phase is more accommodating to local distortions, further facilitating strong optoelectronic bowing. For both structures considered here, a minimum in band gap occurs at Se concentrations slightly below 50% owing to the lower band gap of CdTe in contrast to CdSe. Regarding the implications of these results on PV development, we propose that low-to-intermediate Se concentrations (20–50%) in the zincblende are likely most beneficial given the band gap shown in this region is near that of the ideal value of 1.4 eV according to the Schockley-Queisser limit (Shockley and Queisser, 1961). Furthermore, as discussed in previous works, net photocurrent is also likely to be increased throughout such compositions (Poplawsky et al., 2016).

While the decreased band gap in $CdSe_xTe_{1-x}$ is promising for applications, effective masses (m^*) of electrons and holes are also crucial aspects which influence the net photo-current and therefore the cell efficiency. To this end, the calculated effective masses are shown in Fig. 3(b) and (c), with exact values tabulated in Table S4 of the Supplementary Material. In pure CdTe, we find low effective masses of 0.101 and 0.088 in the zincblende and wurtzite structure respectively, in agreement with previous experimental reports (m^* ranging from 0.096 to 0.11 at free electron densities up to 1.7×10^{18} cm^{-3}) (Mears and Stradling, 1969). These effective electron masses are slightly increased for CdSe, with values of 0.134 and 0.099 in the zincblende and wurtzite structure, owing to increased ionic character and therefore a larger band gap (Vurgaftman et al., 2001). These values also agree with previous experimental work for which an effective electron mass of 0.13 was reported in CdSe (Chemistry R.S.O.).

Throughout intermediate concentrations, we find upward bowing in the electron effective mass, with bowing parameters (δ_{m^*}, calculated via Eq. (2) with p = m^*) of −0.014 and −0.054 in the zincblende and wurtzite structure respectively. The larger changes exhibited by the wurtzite structure can be attributed to stronger structural distortions as discussed earlier in this section. Next, with respect to effective hole mass, we report values of 0.572 and 1.447 for pure CdTe in the zincblende and wurtzite structure respectively. The former lies within the range found by experiment: 0.12 and 0.60 for light and heavy holes in zincblende CdTe (Dang et al., 1982). As with the effective electron masses, these values also increase in CdSe, for which we find hole masses of 0.808 and 1.870 in the zincblende and wurtzite structure respectively. However, in contrast to those of the electrons, effective hole masses display downward bowing throughout intermediate concentrations of $CdSe_xTe_{1-x}$; specifically, bowing parameters (δ_{m^*}) as defined in Eq. (3) are calculated to be 0.14 and 0.47 in the zincblende and wurtzite structure respectively. With respect to applications in PV, the downward bowing effect is favorable given that it allows minimal increases in the effective hole mass, an important parameter for conventional p-type CdTe cells, therefore contributing to potentially higher carrier lifetimes. We also note that focus should remain on the zincblende structure considering the unfavorably large effective hole mass in wurtzite $CdSe_xTe_{1-x}$ throughout all concentrations.

To study the optical properties of $CdSe_xTe_{1-x}$ we focus on the absorption coefficient and reflectivity, each of which are crucial for PV efficiency. The former property is plotted throughout visible-UV photon energies in Fig. 4. In both the zincblende and wurtzite structure, we find first absorption peaks at energies which correlate directly with the corresponding electron band gaps. The rest is due to other transitions and electronic collisions in lattice. Accordingly, features of the full absorption spectra shift toward lower energies at minority Se concentrations (owing to downward bowing in the band gap) and higher energies at majority Se concentrations (as the strong ionic character of the Cd-Se bonds overtakes the bowing effect). Despite these translations, the overall character of the spectra remains relatively unchanged. Hence, zincblende $CdSe_xTe_{1-x}$ is able to maintain strong optical absorption in the range of interest (i.e., at frequencies matching those of the solar spectrum as shown by the shaded region of Fig. 4) whereas the
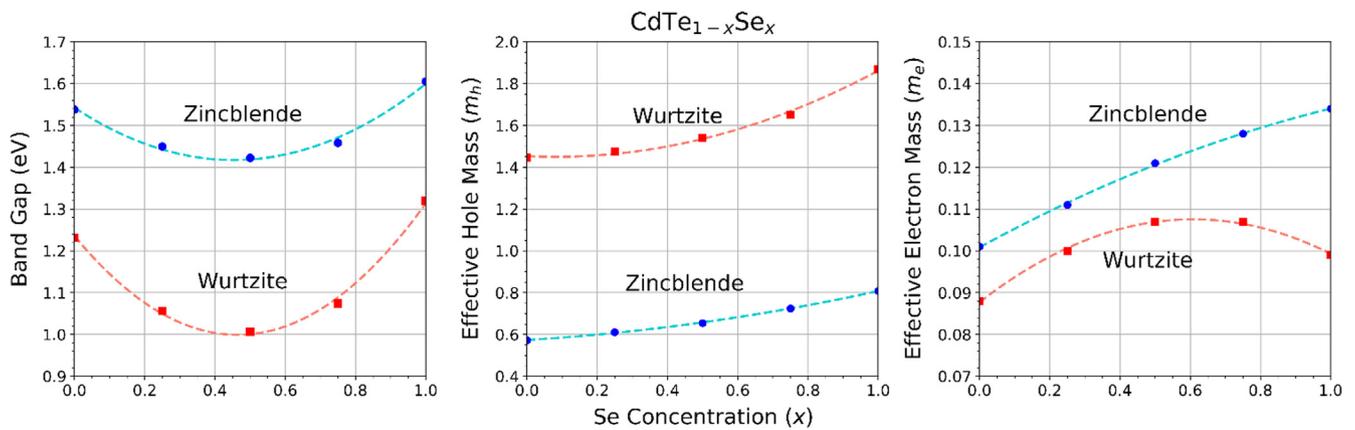
Fig. 3. (a) Electronic band gaps, (b) effective hole masses, and (c) effective electron masses of zincblende and wurtzite $CdTe_{1-x}Se_x$ computed using the hybrid HSE06 functional. Points represent calculated data, whereas dashed curves represent quadratic fitting based on the bowing parameter of each system.
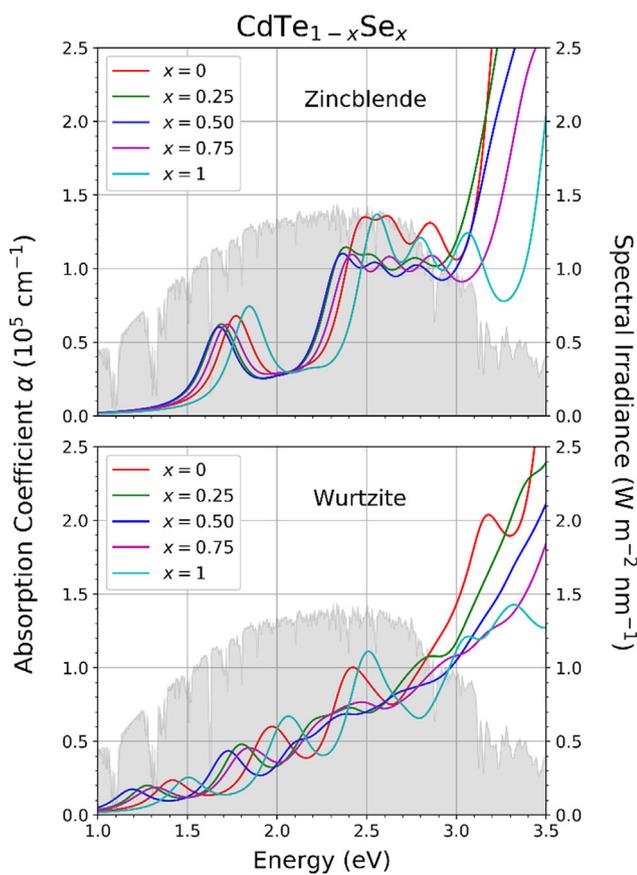

Fig. 4. Absorption coefficients (α) of zincblende (top panel) and wurtzite (bottom panel) $CdTe_{1-x}Se_x$ computed using the hybrid HSE06 functional. Each absorption curve, with values given on left y-axis, corresponds to a given concentration (x). For comparison, the standard AM 1.5 solar spectrum is represented by the shaded area with values given on the right y-axis.

Fig. 5. Reflectivity of zincblende (top panel) and wurtzite (bottom panel) $CdTe_{1-x}Se_x$ computed using the hybrid HSE06 functional. Each reflectivity curve, with values given on left y-axis, corresponds to a given concentration (x).

wurtzite phase consistently displays lower absorption, confirming experimental reports that wurtzite CdTe may be considered optically inactive (Poplawsky et al., 2016). As for reflectivity, for which results are shown in Fig. 5, we find relatively low values ranging from about 0.15 to 0.18 for both the zincblende and wurtzite structure at photon energies below the band gap of each composition. Though there exist variations in reflectivity above the gap, reflectivity generally remains moderate (< 0.35) throughout all optical frequencies in consideration. Moreover, increasing Se concentration leads to noticeable decreases in reflectively across the full spectrum, with downward shifts of
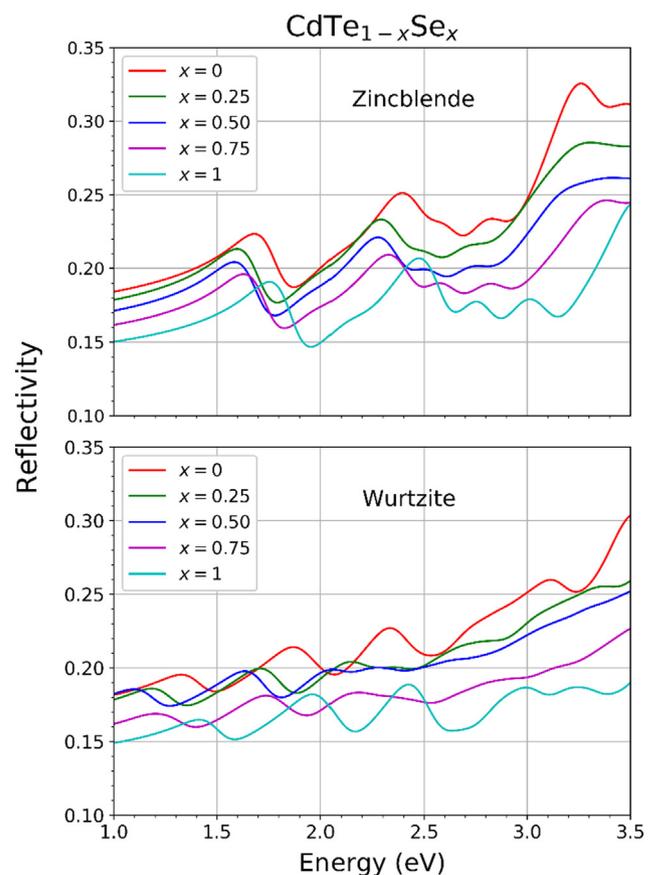
magnitudes approaching 0.05. This slight decrease in reflectivity, coupled with sustained optical absorption, make $CdSe_xTe_{1-x}$ a promising candidate for improved optical performance in PV.

3.3. Short-range order effects

As discussed in detail throughout the work of Bellaiche and Zunger (Bellaiche and Zunger, 1998), there are two major forms of short-range order which typically arise in binary semiconductor alloys: "clustering", for which atoms of the same element tend to congregate with one another, and "anti-clustering", for which atoms of opposing elements tend
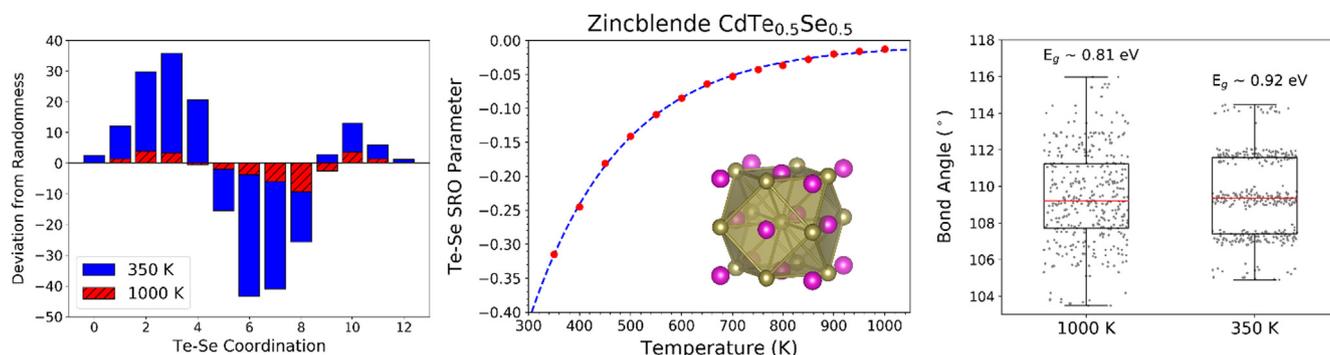
Fig. 6. (a) Occurrences of all possible Te-Se coordination numbers relative to their respective limit in a completely random configuration. Values here are taken from 2048-atom supercells. (b) Short-range order parameter, defined in Eq. (1), of Te-Se pairs in the anion sublattice of disordered $CdSe_{0.5}Te_{0.5}$ simulated at temperatures ranging from 350 K to 1000 K. Negative values imply a deficiency in Te-Se bonds relative to the random limit. (c) Bond angle distributions of $CdSe_{0.5}Te_{0.5}$ simulated at 1000 K and 350 K along with their respective band gaps, calculated using GGA.

to congregate. In this work, we focus on the former effect, which is found to take place in $CdSe_{0.5}Te_{0.5}$. This finding is reflected by our Monte Carlo calculations, revealing the tendency for anion occupations to minimize the total number of Te-Se bond lengths (and therefore maximize nearest-neighbor bonds between atoms of the same element). Such an effect is illustrated in Fig. 6(a); the distribution of Te-Se co-ordination values, relative to the random limit, shows clear deficiencies from 5 to 8 and an abundance above and below this range. We note that intermediate values (i.e., 5–8) serve to maximize the net number of Te-Se bonds whereas high and low values minimize these bonds. There-fore, the results indicate clustering of Te and Se atoms within the dis-ordered $CdSe_{0.5}Te_{0.5}$ structure. This conclusion is further supported by calculations involving Eq. (1); Fig. 6(b) displays the short-range order parameter (σ) throughout temperatures ranging from 350 K to 1000 K. At 350 K, which lies only slightly above the predicted consolute tem-perature, our calculated $\sigma \approx -0.32$ implies a significant presence of short-range order. Specifically, the negative value for σ corresponds to a lower number of Te-Se bonds as compared to the random limit, i.e., clustering is observed. With respect to temperature, we identify an exponential decrease in short-range order which approaches zero at high temperatures, as shown by the exponential least squares regression (dashed line) which closely follows our calculated data as in Fig. 6(b). This agrees with expectations and general data for alloys in the litera-ture (Bellaiche and Zunger, 1998; Ghosh et al., 2008; Körmann et al., 2014); higher temperatures provide sufficient entropic contributions such that configurational disorder dominates the unfavorable energetic effects of enthalpy due to bond length distortions.

To this end, we further study the origin of short-range order by sampling two configurations of $CdSe_{0.5}Te_{0.5}$, simulated using ATAT at 350 K and 1000 K, in order to discern differences between the two ex-treme cases, i.e., with and without short-range order. Bond angle (de-fined as the anion-Cd-anion angle for adjacent anions within each tet-rahedra) distributions of each fully relaxed structure are shown in Fig. 6(c). At 1000 K, our results show a wide and continuous range of bond angles, for which the distribution is centered at approximately 109.5° (the ideal value for a tetrahedra) and occupies values from about 103.5° to 116°. These features are indicative of a random solid solution with significant strain, captured by relaxation in DFT simulations, present in the system. In contrast, the structure simulated at 350 K displays a narrower range of bond angles (approximately 105–114°), also centered at 109.5°, with clear grouping observed around several values. These properties reflect the presence of short-range order, agreeing with our previous analysis, which we may now attribute to reduced strain and therefore decreased enthalpy.

Lastly, we consider the effects of short-range order on the optoe-lectronic properties by calculating the band gap of the representative systems for zincblende $CdSe_{0.5}Te_{0.5}$ at 350 K and 1000 K. These eva-luations were carried out using GGA to avoid excessive computational

costs for such large supercells. Regardless of the method, we may compare these values to those of $CdSe_xTe_{1-x}$ also found using GGA. As tabulated in Fig. 6(c), our calculations reveal noticeably different band gaps of 0.92 eV and 0.81 eV for the structures at 350 K and 1000 K re-spectively. We note that the latter value is in perfect agreement with that of the SQS for $CdSe_{0.5}Te_{0.5}$, hence supporting the conclusion that the structure is almost completely disordered at 1000 K. In contrast, the 0.92 eV gap at 350 K is much closer to the linear combination of the end-member gaps (i.e., if now bowing effects were present), which is found to be about 0.98 eV. As discussed throughout Section 3.2, bowing is known to arise from local structural distortions in the disordered alloy. However, as short-range order serves to minimize these distor-tions, the bowing effects are significantly decreased, thus leading to an increased band gap of 0.92 eV.

4. Conclusion

In summary, we have conducted a thorough study of the structural, thermodynamic, and optoelectronic properties of $CdSe_xTe_{1-x}$ alloys in the zincblende and wurtzite structure. Our calculated phase diagram confirms experimental data showing an upper consolute temperature of 325 K while further clarifying the features of this miscibility boundary throughout the full range of Se concentrations. Above 325 K, we report a downward sloping zincblende-to-wurtzite phase boundary ranging from x = 0.5–0.6 which is attributed to increasing ionic character of the Cd-anion bonds, for which the wurtzite structure is preferred, as more Se atoms are introduced into the system. Moreover, we suggest the critical importance of entropic contributions in stabilizing the phase boundary within this region.

By modeling the purely random configuration of $CdSe_xTe_{1-x}$ through special quasirandom structures, we illustrate significant structural distortions through analysis of nearest- and second-nearest neighbor bond length distributions, each of which occupy a wide range of values. As a result, we observe strong bowing throughout all elec-tronic properties in focus, namely, band gaps and effective electron/hole masses. Despite the band gap of CdSe being larger than that of CdTe for either structure, downward bowing allows a decrease in band gap at low to moderate Se concentrations. Our findings suggest that alloying zincblende $CdSe_xTe_{1-x}$ throughout x = 0.2–0.5 is likely to provide the most beneficial effects for photovoltaics given the band gap within this range is near the ideal value of 1.4 eV, which may also allow enhanced net photocurrent. Furthermore, downward bowing in the effective hole mass should also prevent any substantial decrease in the carrier mobility and therefore carrier mobility may remain high. In terms of optical properties, we identify shifts in the absorption spectra of zincblende and wurtzite $CdSe_xTe_{1-x}$ according to the change in band gap, while the general features remain unchanged. The former structure is found to be more optically active throughout phonon frequencies of

interest. Reflectivity is also studied, for which we find increased Se concentrations lead to a slight decrease in reflectively, hence further improving the potential benefits of these alloys for photovoltaics. We recommend experimental investigation to confirm the subtle changes in optoelectronic properties reported here.

Lastly, investigation of short-range order has revealed the presence of strong clustering (i.e., congregation of like atoms) in $CdSe_xTe_{1-x}$ as illustrated by nearest-neighbor anion-anion bond analysis. The degree of short-range order, which serves to minimize strain, is shown to be high ($\sigma \approx -0.32$) at temperatures shortly above the consolute temperature, while decreasing exponentially with increasing temperature and approaching zero near 1000 K. We show that clustering leads to a larger band gap in the alloy owing to lessened structural distortions and therefore weaker bowing effects. Specifically, the magnitude of the gap in zincblende $CdSe_{0.5}Te_{0.5}$ ranges from 0.81 eV (at 1000 K) to 0.92 eV (at 350 K) within the framework of GGA. Therefore, we propose that, in addition to composition, short-range order may be utilized experimentally to finely tune the desired optoelectronic properties of the material. This may achieved by carrying out synthesis under thermal conditions giving a desired degree of clustering, according to the detailed trends reported here, followed by quenching to sufficiently low temperatures to "freeze in" local occupations within the structure (see, e.g., reference Ji et al. (2019)).

Acknowledgement

Disclaimer

The views and conclusions contained herein are those of the authors and should not be interpreted as necessarily representing the official policies or endorsements, either expressed or implied, of Air Force Research Laboratory or the U.S. Government.

Appendix A. Supplementary material

Supplementary data to this article can be found online at https://doi.org/10.1016/j.solener.2019.10.091.

References

Allred, A.L., Rochow, E.G., 1958. A scale of electronegativity based on electrostatic force. J. Inorg. Nucl. Chem. 5 (4), 264–268.

Baines, T., et al., 2018. Incorporation of CdSe layers into CdTe thin film solar cells. Sol. Energy Mater. Sol. Cells 180, 196–204.

Balasubramanian, K., Khare, S., Gall, D., 2016. Vacancy-induced mechanical stabilization of cubic tungsten nitride. Phys. Rev. B 94 (17), 174111.

Bellaiche, L., Zunger, A., 1998. Effects of atomic short-range order on the electronic and optical properties of GaAsN, GaInN, and GaInAs alloys. Phys. Rev. B 57 (8), 4425.

Belyaev, A., Kalinkin, I., 1988. Conduction processes in inhomogeneous $CdSe_xTe_{1-x}$ semiconductors. Thin Solid Films 158 (1), 25–36.

Blochl, P.E., 1994. Projector augmented-wave method. Phys. Rev. B 50 (24), 17953–17979.

Blöchl, P.E., Jepsen, O., Andersen, O.K., 1994. Improved tetrahedron method for Brillouin-zone integrations. Phys. Rev. B 49 (23), 16223–16233.

Cai, X.C., et al., 2012. Spectroscopy of CdTe/CdSe type-II nanostructures: morphology, lattice mismatch, and band-bowing effects. J. Phys. Chem. C 116 (14), 8118–8127.

Chemistry, R.S.O. Available from: < http://www.rsc.org/suppdata/cp/c3/c3cp52678j/c3cp52678j.pdf > .

Compaan, D., et al., 1996. Properties of pulsed laser deposited CdS_xTe_{1-x} films on glass. MRS Proc. 426, 367.

Computer, O.S. Available from: < https://www.osc.edu/ > .

Dang, L.S., Neu, G., Romestain, R., 1982. Optical detection of cyclotron resonance of electron and holes in CdTe. Solid State Commun. 44 (8), 1187–1190.

De Fontaine, D., 1994. Cluster approach to order-disorder transformations in alloys. In: Solid State Physics. Elsevier, pp. 33–176.

Deringer, V.L., Tchougreeff, A.L., Dronskowski, R., 2011. Crystal orbital hamilton population (COHP) analysis as projected from plane-wave basis sets. J. Phys. Chem. A 115 (21), 5461–5466.

Ducastelle, F., Ducastelle, F., 1991. Order and phase stability in alloys.

Dünweg, B., Landau, D., 1993. Phase diagram and critical behavior of the Si-Ge unmixing transition: a Monte Carlo study of a model with elastic degrees of freedom. Phys. Rev. B 48 (19), 14182.

Geisthardt, R.M., Topic, M., Sites, J.R., 2015. Status and potential of CdTe solar-cell efficiency. IEEE J. Photovoltaics 5 (4), 1217–1221.

Gessert, T.A., et al., 2013. Research strategies toward improving thin-film CdTe photovoltaic devices beyond 20% conversion efficiency. Sol. Energy Mater. Sol. Cells 119, 149–155.

Ghosh, G., Van de Walle, A., Asta, M., 2008. First-principles calculations of the structural and thermodynamic properties of bcc, fcc and hcp solid solutions in the Al–TM (TM = Ti, Zr and Hf) systems: a comparison of cluster expansion and supercell methods. Acta Mater. 56 (13), 3202–3221.

Gibbs, Z.M., et al., 2017. Effective mass and Fermi surface complexity factor from ab initio band structure calculations. NPJ Comput. Mater. 3, 7.

Gloeckler, M., Sankin, I., Zhao, Z., 2013. CdTe solar cells at the threshold to 20% efficiency. IEEE J. Photovoltaics 3 (4), 1389–1393.

Granas, O., Vinichenko, D., Kaxiras, E., 2016. Establishing the limits of efficiency of perovskite solar cells from first principles modeling. Sci. Rep. 6, 6.

Green, M.A., et al., 2018. Solar cell efficiency tables (version 51). Prog. Photovoltaics Res. Appl. 26 (1), 3–12.

Hannachi, L., Bouarissa, N., 2008. Electronic structure and optical properties of $CdSe_xTe_{1-x}$ mixed crystals. Superlattices Microstruct. 44 (6), 794–801.

Heermann, K.B.A.D., 1988. Monte Carlo Simulation in Statistical Physics. Springer-Verlag, New York.

Henkelman, G., Arnaldsson, A., Jonsson, H., 2006. A fast and robust algorithm for Bader decomposition of charge density. Comput. Mater. Sci. 36 (3), 354–360.

Heyd, J., et al., 2005. Energy band gaps and lattice parameters evaluated with the Heyd-Scuseria-Ernzerhof screened hybrid functional. J. Chem. Phys. 123 (17), 174101.

Heyd, J., Scuseria, G.E., Ernzerhof, M., 2003. Hybrid functionals based on a screened Coulomb potential. J. Chem. Phys. 118 (21), 8207–8215.

Hosseini, S.M., 2008. Optical properties of cadmium telluride in zinc-blende and wurzite structure. Phys. B – Condens. Matter 403 (10–11), 1907–1915.

Huang, M.-Z., Ching, W.Y., 1993. Calculation of optical excitations in cubic semiconductors. I. Electronic structure and linear response. Phys. Rev. B 47 (15), 9449–9463.

Islam, R., Banerjee, H., Rao, D., 1995. Structural and optical properties of $CdSe_xTe_{1-x}$ thin films grown by electron beam evaporation. Thin Solid Films 266 (2), 215–218.

Ito, T., 1998. Simple criterion for Wurtzite-Zinc-Blende polytypism in semiconductors. Jpn. J. Appl. Phys. 37 (Part 2(10B), L1217–L1220.

Jain, A., et al., 2013. Commentary: the materials project: a materials genome approach to accelerating materials innovation. APL Mater. 1 (1), 11.

Jamal, M., Abu-Jafar, M.S., Reshak, A.H., 2016. Revealing the structural, elastic and thermodynamic properties of CdSexTe1−x (x = 0, 0.25, 0.5, 0.75, 1). J. Alloys Compd. 667, 151–157.

Ji, H., et al., 2019. Hidden structural and chemical order controls lithium transport in cation-disordered oxides for rechargeable batteries. Nat. Commun. 10 (1), 592.

Kaczkowski, J., 2012. Electronic structure of some wurtzite semiconductors: hybrid functionals vs. Ab initio many body calculations. GaN 3 (3.130), p. 3.103.

Kale, R.B., Lokhande, C.D., 2004. Band gap shift, structural characterization and phase transformation of CdSe thin films from nanocrystalline cubic to nanorod hexagonal on air annealing. Semicond. Sci. Technol. 20 (1), 1–9.

Kanevce, A., et al., 2017. The roles of carrier concentration and interface, bulk, and grain-boundary recombination for 25% efficient CdTe solar cells. J. Appl. Phys. 121 (21), 9.

Kasper, E., et al., 1995. Test of Vegard's law in thin epitaxial SiGe layers. J. Cryst. Growth 157 (1), 68–72.

Kim, Y.-I., Page, K., Seshadri, R., 2007. Synchrotron x-ray study of polycrystalline wurtzite Zn1−xMgxO (0⩽x⩽0.15): Evolution of crystal structure and polarization. Appl. Phys. Lett. 90(10), 101904.

Körmann, F., et al., 2014. Temperature dependent magnon-phonon coupling in bcc Fe from theory and experiment. Phys. Rev. Lett. 113 (16), 165503.

Kresse, G., Furthmuller, J., 1996. Efficient iterative schemes for ab initio total-energy calculations using a plane-wave basis set. Phys. Rev. B 54 (16), 11169–11186.

Kresse, G., Furthmuller, J., 1996. Efficiency of ab-initio total energy calculations for metals and semiconductors using a plane-wave basis set. Comput. Mater. Sci. 6 (1), 15–50.

Kresse, G., Hafner, J., 1993. Ab initio molecular dynamics for liquid metals. Phys. Rev. B 47 (1), 558–561.

Kresse, G., Hafner, J., 1994. Ab initio molecular-dynamics simulation of the liquid-metal–amorphous-semiconductor transition in germanium. Phys. Rev. B 49 (20), 14251.

Kresse, G., Joubert, D., 1999. From ultrasoft pseudopotentials to the projector augmented-wave method. Phys. Rev. B 59 (3), 1758–1775.

Krukau, A.V., et al., 2006. Influence of the exchange screening parameter on the performance of screened hybrid functionals. J. Chem. Phys. 125 (22), 224106.

Laradji, M., Landau, D., Dünweg, B., 1995. Structural properties of $Si_{1-x}Ge_x$ alloys: a Monte Carlo simulation with the Stillinger-Weber potential. Phys. Rev. B 51 (8), 4894.

Laugier, A., 1973. Thermodynamics and phase diagram calculations in II-VI and IV-VI

ternary systems using an associated solution model. Rev. Phys. Appl. (Paris) 8 (3), 259–270.

Lingg, M., et al., 2018. Structural and electronic properties of CdTe$_{1-x}$Se$_x$ films and their application in solar cells. Sci. Technol. Adv. Mater. 19 (1), 683–692.

Liu, Z.T.Y., et al., 2017. First-principles phase diagram calculations for the rocksalt-structure quasibinary systems TiN-ZrN, TiN-HfN and ZrN-HfN. J. Phys. – Condens. Matter 29 (3), 11.

Madsen, G.K.H., Singh, D.J., 2006. BoltzTraP. A code for calculating band-structure dependent quantities. Comput. Phys. Commun. 175 (1), 67–71.

Magnusson, K.O., et al., 1987. Angle-resolved inverse photoelectron spectroscopy studies of CdTe (110), CdS (112¯ 0), and CdSe (112¯ 0). Phys. Rev. B 36 (12), 6566–6573.

Maintz, S., et al., 2013. Analytic projection from plane-wave and PAW wavefunctions and application to chemical-bonding analysis in solids. J. Comput. Chem. 34 (29), 2557–2567.

Maintz, S., et al., 2016. LOBSTER: a tool to extract chemical bonding from plane-wave based DFT. J. Comput. Chem. 37 (11), 1030–1035.

Maintz, S., Esser, M., Dronskowski, R., 2016. Efficient rotation of local basis functions using real spherical harmonics. Acta Phys. Pol. B 47 (4), 1165–1175.

Mangalhara, J., Thangaraj, R., Agnihotri, O., 1989. Structural, optical and photoluminescence properties of electron beam evaporated CdSe$_{1-x}$Te$_x$ films. Solar Energy Mater. 19 (3–5), 157–165.

McCandless, B.E., et al., 2018. Overcoming carrier concentration limits in polycrystalline CdTe thin films with in situ doping. Sci. Rep. 8 (1), 14519.

Mears, A.L., Stradling, R.A., 1969. Cyclotron resonance and cross-modulation with n-type CdTe at 1 mm and 2 mm wavelength. Solid State Commun. 7 (17), 1267–1269.

Moses, P.G., et al., 2011. Hybrid functional investigations of band gaps and band alignments for AlN, GaN, InN, and InGaN. J. Chem. Phys. 134 (8), 084703.

Murali, K.R., Jayasuthaa, B., 2009. Brush electrodeposited CdSe$_x$Te$_{1-x}$ thin films and their properties. Sol. Energy 83 (6), 891–895.

Newman, M., Barkema, G., 1999. Monte Carlo Methods in statistical physics chapter 1–4. Oxford University Press, New York, USA.

Ong, S.P., et al., 2013. Python Materials Genomics (pymatgen): A robust, open-source python library for materials analysis. Comput. Mater. Sci. 68, 314–319.

Ouendadji, S., et al., 2011. Ab initio study of structural, electronic, phase diagram, and optical properties of CdSe$_x$Te$_{1-x}$ semiconducting alloys. J. Mater. Sci. 46 (11), 3855–3861.

Ozolins, V., Wolverton, C., Zunger, A., 1998. First-principles theory of vibrational effects on the phase stability of Cu-Au compounds and alloys. Phys. Rev. B 58 (10), R5897–R5900.

Paier, J., et al., 2006. Screened hybrid density functionals applied to solids. J. Chem. Phys. 124 (15), 13.

Paudel, N.R., Yan, Y., 2014. Enhancing the photo-currents of CdTe thin-film solar cells in both short and long wavelength regions. Appl. Phys. Lett. 105 (18), 183510.

Perdew, J.P., et al., 1992. Atoms, molecules, solids, and surfaces - applications of the generalized gradient approximation for exchange and correlation. Phys. Rev. B 46 (11), 6671–6687.

Perdew, J.P., et al., 1993. Erratum: atoms, molecules, solids, and surfaces: applications of the generalized gradient approximation for exchange and correlation. Phys. Rev. B 48 (7), 4978.

Perrenoud, J., et al., 2013. A comprehensive picture of Cu doping in CdTe solar cells. J. Appl. Phys. 114 (17), 10.

Poon, H.C., et al., 1995. Relativistic band structure of ternary II-VI semiconductor alloys containing Cd, Zn, Se and Te. J. Phys.: Condens. Matter 7 (14), 2783–2799.

Poplawsky, J.D., et al., 2015. CdSe$_{1-x}$Te$_x$ phase segregation in CdSe/CdTe based solar cells. Microsc. Microanal. 21 (S3), 691–692.

Poplawsky, J.D., et al., 2016. Structural and compositional dependence of the CdTe$_x$Se$_{1-x}$ alloy layer photoactivity in CdTe-based solar cells. Nat. Commun. 7, 12537.

Porter, D., Easterling, K., Easterling, K., 2009. Phase Transformations in Metals and Alloys. CRC Press, Boca Raton.

Pyykkö, P., 2015. Additive covalent radii for single-, double-, and triple-bonded molecules and tetrahedrally bonded crystals: a summary. J. Phys. Chem. A 119 (11), 2326–2337.

Reshak, A.H., et al., 2011. Effect of increasing tellurium content on the electronic and optical properties of cadmium selenide telluride alloys CdSe$_{1-x}$Te$_x$: An ab initio study. J. Alloy. Compd. 509 (24), 6737–6750.

Roehl, J.L., Khare, S.V., 2014. Diffusion of Te vacancy and interstitials of Te, Cl, O, S, P and Sb in CdTe: A density functional theory study. Sol. Energy Mater. Sol. Cells 128, 343–350.

Roehl, J.L., Khare, S.V., 2014. Diffusion of Cd vacancy and interstitials of Cd, Cu, Ag, Au and Mo in CdTe: A first principles investigation. Sol. Energy 101, 245–253.

Roehl, J.L., Liu, Z.T.Y., Khare, S.V., 2014. Diffusion in CdS of Cd and S vacancies and Cu,

Cd, Cl, S and Te interstitials studied with first-principles computations. Mater. Res. Express 1 (2), 025904.

Romeo, N., et al., 2004. Recent progress on CdTe/CdS thin film solar cells. Sol. Energy 77 (6), 795–801.

Sanchez, J.M., Ducastelle, F., Gratias, D., 1984. Generalized cluster description of multicomponent systems. Physica A 128 (1–2), 334–350.

Sanville, E., et al., 2007. Improved grid-based algorithm for Bader charge allocation. J. Comput. Chem. 28 (5), 899–908.

Schenk, M., 1998. Zusammenfassung und Ausblick, in Altautomobilrecycling: Technisch-ökonomische Zusammenhänge und wirtschaftspolitische Implikationen. Deutscher Universitätsverlag, Wiesbaden, pp. 295–297.

Shakil, M., et al., 2016. Theoretical calculations of structural, electronic, and elastic properties of CdSe$_{1-x}$Te$_x$: A first principles study. Chin. Phys. B 25 (7), 7.

Shockley, W., Queisser, H.J., 1961. Detailed balance limit of efficiency of p-n junction solar cells. J. Appl. Phys. 32 (3), 510–519.

Strauss, A.J., Steininger, J., 1970. Phase diagram of the CdTe-CdSe pseudobinary system. J. Electrochem. Soc. 117 (11), 1420–1426.

Swanson, D.E., Sites, J.R., Sampath, W.S., 2017. Co-sublimation of CdSe$_x$Te$_{1-x}$ layers for CdTe solar cells. Sol. Energy Mater. Sol. Cells 159, 389–394.

Szemjonov, A., et al., 2014. Investigation of the bulk and surface properties of CdSe: insights from theory. PCCP 16 (42), 23251–23259.

Tang, W., Sanville, E., Henkelman, G., 2009. A grid-based Bader analysis algorithm without lattice bias. J. Phys.-Condens., Matter 21 (8), 7.

Terheggen, M., et al., 2004. Analysis of bulk and interface phenomena in CdTe/CdS thin-film solar cells. Interface Sci. 12 (2–3), 259–266.

Tit, N., Obaidat, I.M., Alawadhi, H., 2009. Origins of bandgap bowing in compound-semiconductor common-cation ternary alloys. J. Phys.: Condens. Matter 21 (7), 075802.

Uthanna, S., Reddy, P.J., 1983. Structural and electrical properties of CdSe$_x$Te$_{1-x}$ thin films. Solid State Commun. 45 (11), 979–980.

van de Walle, A., 2009. Multicomponent multisublattice alloys, nonconfigurational entropy and other additions to the Alloy Theoretic Automated Toolkit. Calphad-Computer Coupling Phase Diagrams Thermochem. 33 (2), 266–278.

van de Walle, A., 2013. Methods for first-principles alloy thermodynamics. JOM 65 (11), 1523–1532.

van de Walle, A., Asta, M., 2002. Self-driven lattice-model Monte Carlo simulations of alloy thermodynamic properties and phase diagrams. Modell. Simul. Mater. Sci. Eng. 10 (5), 521–538.

van de Walle, A., Ceder, G., 2002. Automating first-principles phase diagram calculations. J. Phase Equilibria 23 (4), 348–359.

van de Walle, A., Ceder, G., 2002. The effect of lattice vibrations on substitutional alloy thermodynamics. Rev. Mod. Phys. 74 (1), 11–45.

van de Walle, A., Asta, M., Ceder, G., 2002. The alloy theoretic automated toolkit: a user guide. Calphad-Computer Coupling Phase Diagrams Thermochem. 26 (4), 539–553.

van Swol, F., et al., 2016. Thermodynamic properties of model CdTe/CdSe mixtures. Mol. Simul. 42 (1), 14–24.

Vegard, L., 1921. Die Konstitution der Mischkristalle und die Raumfüllung der Atome. Zeitschrift für Physik 5 (1), 17–26.

Vurgaftman, I., Meyer, J.á., Ram-Mohan, L.á., 2001. Band parameters for III–V compound semiconductors and their alloys. J. Appl. Phys. 89(11), 5815–5875.

Vurgaftman, I., Meyer, J.R., Ram-Mohan, L.R., 2001. Band parameters for III–V compound semiconductors and their alloys. J. Appl. Phys. 89 (11), 5815–5875.

Warner, J., et al., 2006. Ab initio calculations for properties of MAX phases Ti$_2$TlC, Zr$_2$TlC, and Hf$_2$TlC. Appl. Phys. Lett. 88 (10), 101911.

Yang, J., Wei, S.-H., 2019. Enhancing CdTe solar cell performance by reducing the ideal bandgap of CdTe through CdTe1 − xSex alloying. arXiv e-prints.

Yeh, C.-Y., et al., 1992. Zinc-blende–wurtzite polytypism in semiconductors. Phys. Rev. B 46 (16), 10086–10097.

Yu, M., Trinkle, D.R., 2011. Accurate and efficient algorithm for Bader charge integration. J. Chem. Phys. 134 (6), 8.

Zhao, Y., et al., 2016. Monocrystalline CdTe solar cells with open-circuit voltage over 1 V and efficiency of 17%. Nat. Energy 1, 16067.

Zhou, X., Gall, D., Khare, S.V., 2014. Mechanical properties and electronic structure of anti-ReO$_3$ structured cubic nitrides, M$_3$N, of d block transition metals M: An ab initio study. J. Alloy. Compd. 595, 80–86.

Zunger, A., et al., 1990. Special quasirandom structures. Phys. Rev. Lett. 65 (3), 353–356.

Zunger, A., 1994. *First-principles statistical mechanics of semiconductor alloys and intermetallic compounds*. In: *Statics and Dynamics of Alloy Phase* Transformations. Springer, pp. 361–419.

Zweibel, K.E.N., 1992. Toward low cost CdTe PV. Int. J. Sol. Energy 12 (1–4), 285–292.